Crack elimination and strength enhancement mechanisms of selective laser melted Si-modified Al−Mn−Mg−Er−Zr alloy

Jiang YU[1], Yao-xiang GENG[1], Hong-bo JU[1,2], Zhi-jie ZHANG[1], Jun-hua XU[1]

1. School of Materials Science and Engineering, Jiangsu University of Science and Technology,
Zhenjiang 212100, China;
2. Department of Mechanical Engineering, CEMMPRE-Centre for Mechanical Engineering Materials and Processes,
University of Coimbra, Coimbra, Portugal

Abstract: In order to increase the processability and process window of the selective laser melting (SLM)-fabricated Al−Mn−Mg−Er−Zr alloy, a novel Si-modified Al−Mn−Mg−Er−Zr alloy was designed. The effect of Si alloying on the surface quality, processability, microstructure, and mechanical properties of the SLM-fabricated alloy was studied. The results showed that introducing Si into the Al−Mn−Mg−Er−Zr alloy prevented balling and keyhole formation, refined the grain size, and reduced the solidification temperature, which eliminated cracks and increased the processability and process window of the alloy. The maximum relative density of the SLM-fabricated Si/Al−Mn−Mg−Er−Zr alloy reached 99.6%. The yield strength and ultimate tensile strength of the alloy were (371±7) MPa and (518±6) MPa, respectively. These values were higher than those of the SLM-fabricated Al−Mn−Mg−Er−Zr and other Sc-free Al−Mg-based alloys.
Key words: selective laser melting; Al−Mn−Mg−Er−Zr−Si alloy; surface roughness; processability; mechanical properties

1 Introduction

Selective laser melting (SLM) is one of the most widely-used additive manufacturing technologies for obtaining metal parts with complex geometries that are unachievable by traditional manufacturing methods. In addition, the rapid cooling nature of SLM technology provides a high solid solubility of alloying elements and a fine microstructure far beyond the traditional process, thus improving the mechanical properties of manufactured parts [1−3].

In the SLM-fabricated Al−Mg/Mn-based alloys, the introduction of Sc and Zr alloying elements prevents the formation of solidification cracks and improves the strength of the base alloy through fine-grain strengthening and precipitation strengthening from the decomposition of Al₃Sc and/or Al₃(Sc,Zr) precipitates [4−6]. Scalmalloy® (Al−4.50Mg−0.51Mn−0.66Sc−0.37Zr) was first designed for SLM by introducing high content Sc and Zr elements into Al−Mg−Sc−Zr alloy according to the advantages of non-equilibrium metallurgical features of the SLM process [7]. This alloy exhibited a high yield strength (YS) of 520 MPa and an ultimate tensile strength (UTS) of 530 MPa after direct aging treatment at 325 °C for 4 h due to the precipitation of high-density secondary Al₃Sc nanoparticles [8], which were much higher than those of conventional wrought Al−Mg−Sc−Zr alloy [9]. To further increase the strength of the SLM-fabricated Al−Mg−Mn−Sc−Zr alloy, GENG et al [10−12] designed an ultra-high strength

Al−Mn−Mg−Sc−Zr alloy with high contents of (Mg+Mn) and (Sc+Zr). Both the YS and UTS of the alloy exceeded 600 MPa after direct aging treatment. However, the high levels of Sc in raw materials increased the costs of the alloy powder. Erbium has been proposed as an alternative element that possesses similar characteristics to Sc, which can also form $L1_2$-type precipitates to improve the mechanical properties of aluminum alloys [13−15]. The price of Er is only one-thirtieth that of Sc. In our previous work [16], a novel Sc-free Al−Mn−Mg−Er−Zr alloy was fabricated by SLM. The alloy showed good mechanical properties with YS, UTS, and elongation of (327±5) MPa, (502±3) MPa, and (12.2±1)%, respectively. Unfortunately, the alloy exhibited a narrow processing window, and hot cracks existed in most of the SLM-fabricated samples.

The introduction of Si as an alloying element in 2xxx, 7xxx, and 5xxx-series alloys can prevent the formation of cracks during SLM by offering an extra liquid phase to reduce solidification shrinkage [5,17−20]. For instance, MONTERO-SISTIAGA et al [20] introduced 4 wt.% Si into a 7075 alloy to eliminate cracks in the SLM-fabricated alloy. LI et al [5] added 1.3% Si to Al−Mg alloy to reduce the crack susceptibility of SLM-fabricated alloy. In this work, a Si-modified Al−Mn−Mg−Er−Zr alloy was fabricated by SLM. The effect of Si alloying on the surface morphology, processability, microstructure, and mechanical properties of the alloy was studied.

2 Experimental

2.1 Powder material and SLM process

The Al−6.01Mn−2.74Mg−0.86Er−0.52Zr (wt.%) powder was prepared by a vacuum induction N_2 gas atomization process. The chemical composition of the powder was verified by inductively coupled plasma atomic emission spectroscopy. Si/Al−Mn−Mg−Er−Zr composite powder (2 wt.% Si and 98 wt.% Al−6.01Mn−2.74Mg−0.86Er−0.52Zr) was synthesized by mechanical mixing. The scanning electron microscopy (SEM) image, particle size distribution, and energy-dispersive X-ray spectroscopy (EDX) mapping of Si/Al−Mn−Mg−Sc−Zr composite powder are shown in Fig. 1. SLM specimens with a size of 55 mm × 15 mm × 15 mm

were conducted using an EP M260 machine (E-Plus-3D, China). The processing parameters are given in Table 1.

2.2 Microstructure, density and mechanical tests

The top surface topography and microstructure of the SLM-fabricated specimens were examined with scanning electron microscope (SEM, SM-6480, at 200 kV) and optical microscope (OM), respectively. A LEXTOLS4000 laser scanning confocal microscopy (LSCM) was applied to measuring the roughness of the top surface of the specimens. X-ray computed tomography (X-ray CT, GE v/tome/x m) was performed to analyze the volume fraction and morphology of pores of the SLM-fabricated specimens. Electron backscattered diffraction (EBSD) was used to analyze the crystallographic orientation and grain size of the specimens. X-ray diffractometry (XRD) was performed in a D8 advance using a Cu-tube at 40 kV and 40 mA. The thermal analysis of the alloys was characterized by differential thermal analysis (DTA) in a Pyris Diamond with a cooling rate of 20 °C/min. The mass density of specimens was determined using the Archimedes method. A UTM5105 type universal testing machine was used to test tensile property of the alloy at a constant strain rate of 1 mm/min according to the ASTM E8-04 standard.

3 Results

3.1 Surface morphology

The SEM and LSCM top-surface images of Al−Mn−Mg−Er−Zr and Si/Al−Mn−Mg−Er−Zr samples fabricated under different laser powers and scanning speeds are shown in Fig. 2. For the SLM-fabricated Al−Mn−Mg−Er−Zr alloy, balling was observed on all sample surfaces. The diameter of balls varied from tens to hundreds of microns. As a result, the alloy showed a large roughness of 18.573−42.623 μm (Fig. 2(a)). Cracks were also observed on the surface of most samples, as shown in Fig. 2(a). Conversely, balling did not exist on the upper surface of the SLM-fabricated Si/Al−Mn−Mg−Er−Zr alloy (Fig. 2(b)), except for some Er-containing oxide particles with a size of several microns and large elliptical oxide residues induced by spatter spreading (Fig. 3). The roughness of the
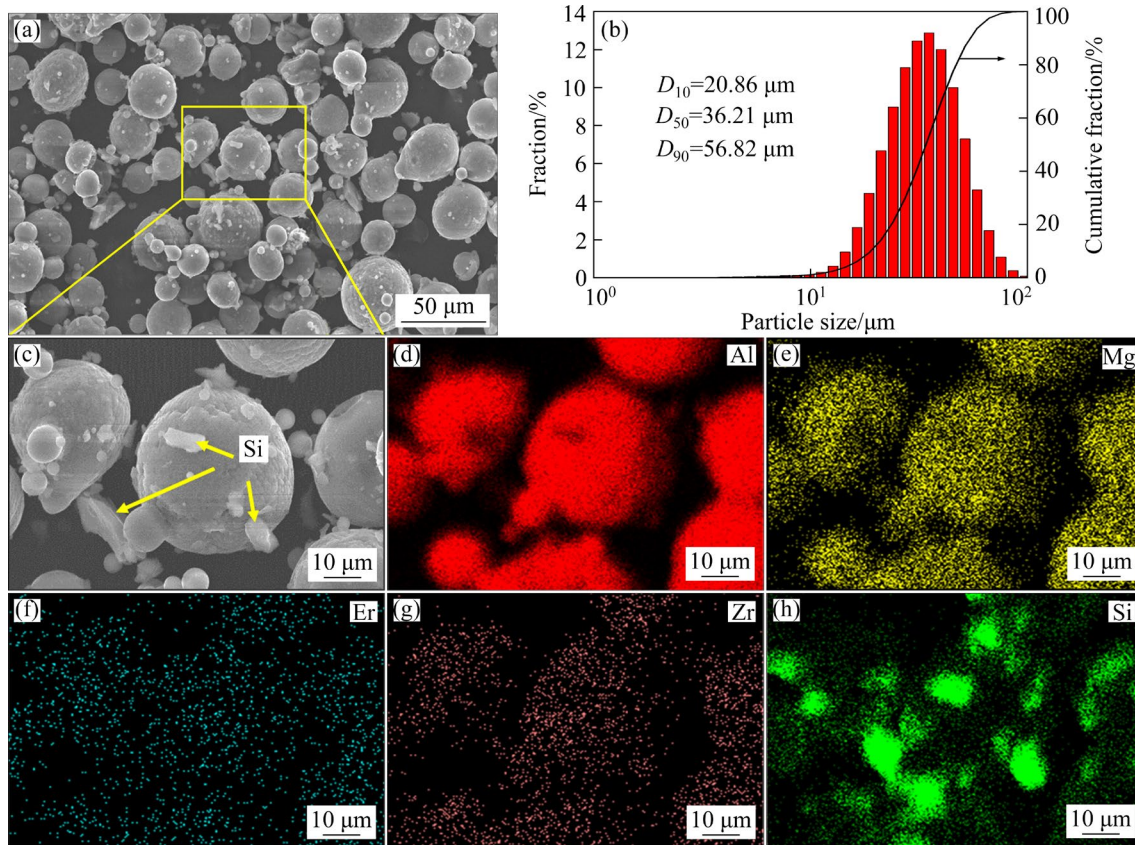
Fig. 1 SEM images (a, c), size distribution (b), and EDX mappings (d−h) of Si/Al−Mn−Mg−Er−Zr composite powder

Table 1 Processing parameters during SLM

Parameter	Value
Laser power/W	250, 350
Laser scan speed/(mm·s^{-1})	800, 900, 1000, 1100, 1200
Laser spot diameter/μm	100
Hatch distance/μm	100
Layer thickness/μm	30

alloy varied in the range of 8.665−21.309 μm under different processing parameters (Fig. 2(b)).

3.2 Microstructure and relative density

OM images of the longitudinal section of the SLM-fabricated Al−Mn−Mg−Er−Zr and Si/Al−Mn−Mg−Er−Zr alloys with different process parameters are shown in Fig. 4. The SLM-fabricated Al−Mn−Mg−Er−Zr samples obtained with only three parameters did not have hot cracks, as shown in Fig. 4(a). Interestingly, after alloying with 2 wt.% Si, no hot cracks were found in any sample (Fig. 4(b)). The relative density of the Al−Mn−Mg−Er−Zr alloys fabricated under

different processes was less than 99%. The highest relative density of about 98.9% was achieved at a laser power of 350 W and a scanning speed of 800 mm/s, as shown in Fig. 5. The relative density of all SLM-fabricated Si/Al−Mn−Mg−Er−Zr alloys exceeded 99.2%, showing a wide process window. The sample fabricated at a laser power of 250 W and a scanning speed of 1000 mm/s exhibited a maximum relative density of 99.6%, showing good processability (Fig. 5). The CT analysis showed that the Al−Mn−Mg−Er−Zr alloy fabricated at a laser power of 350 W and a scanning speed of 800 mm/s exhibited many irregular keyholes and circular metallurgical holes (Fig. 6(a)). However, only a small number of circular holes were found in the SLM-fabricated Si/Al−Mn−Mg−Er−Zr alloy, as shown in Fig. 6(b). This was consistent with the OM and relative density results.

3.3 Phase composition, and thermal analysis results

The XRD patterns showed that α(Al), Al$_3$Er, and Al$_6$Mn phases existed in the SLM-fabricated
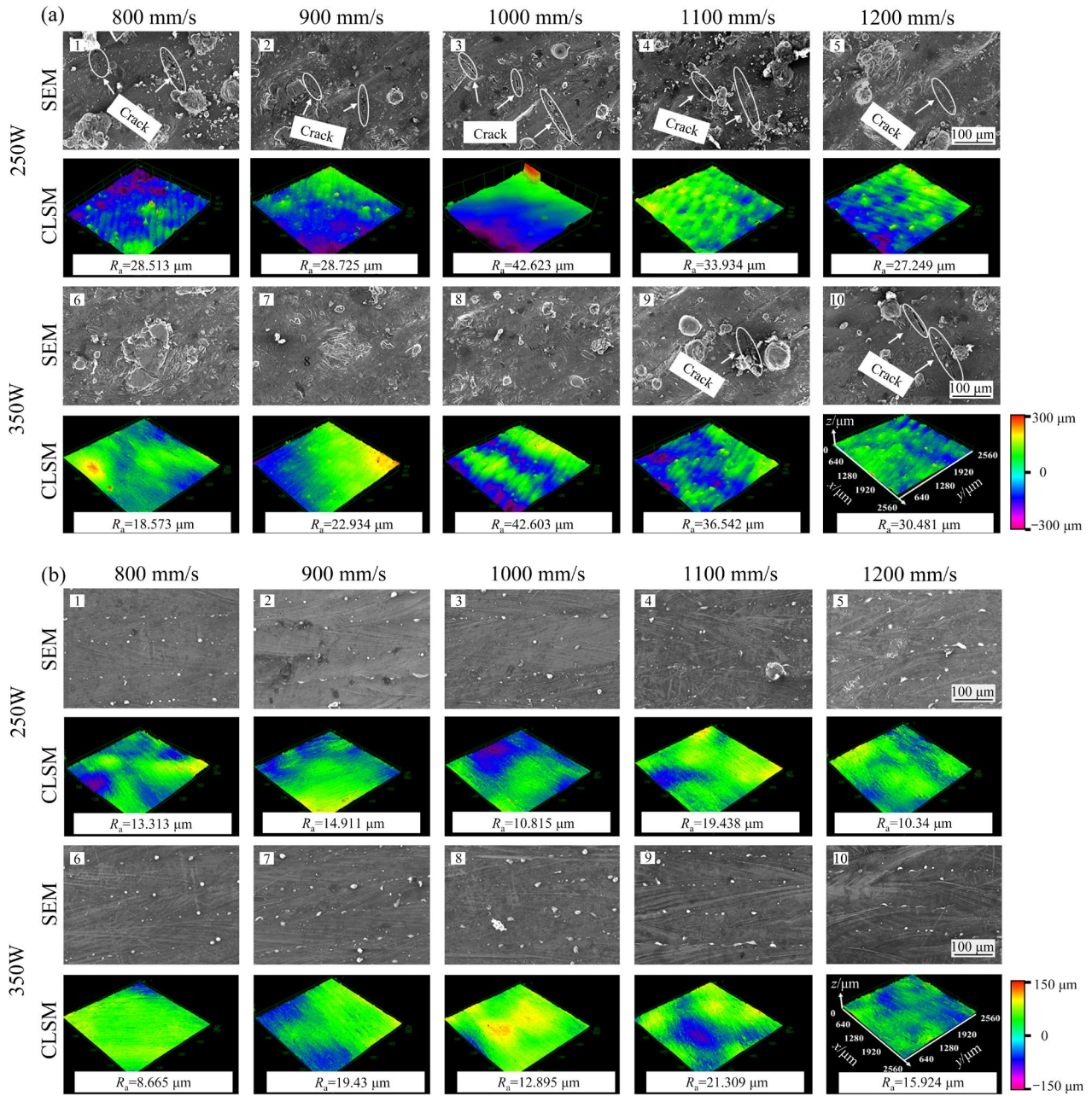
Fig. 2 SEM and LSCM images of upper surface of SLM-fabricated samples under different process conditions: (a) Al−Mn−Mg−Er−Zr; (b) Si/Al−Mn−Mg−Er−Zr
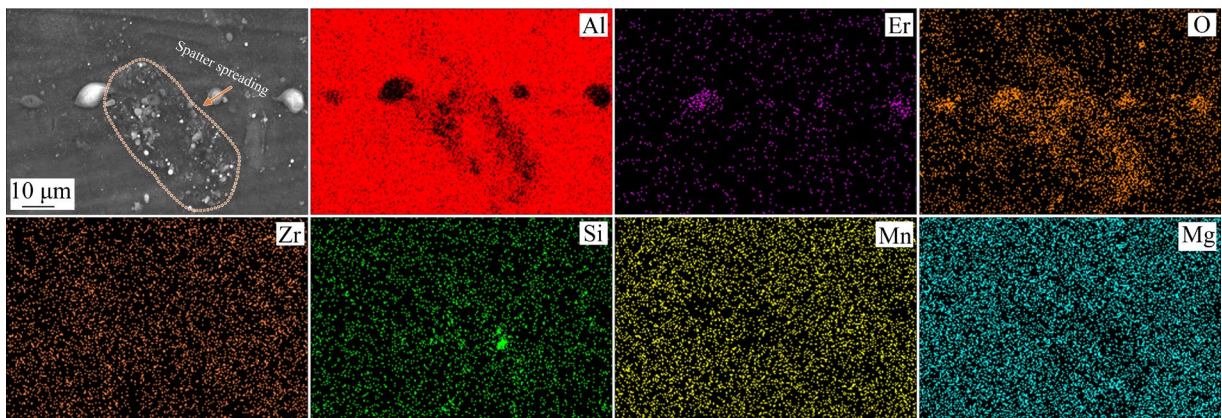

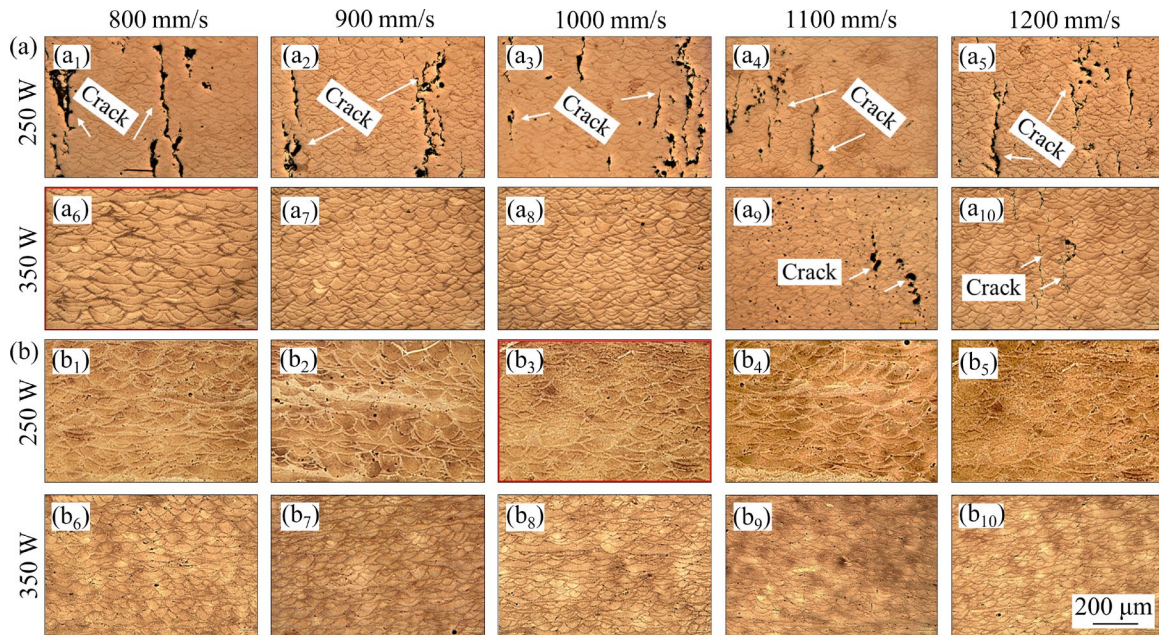**Fig. 3** EDX mappings of upper surface of SLM-fabricated Si/Al−Mn−Mg−Er−Zr samples

Fig. 4 OM images of SLM-fabricated Al−Mn−Mg−Er−Zr (a) and Si/Al−Mn−Mg−Er−Zr (b) samples with different process parameters
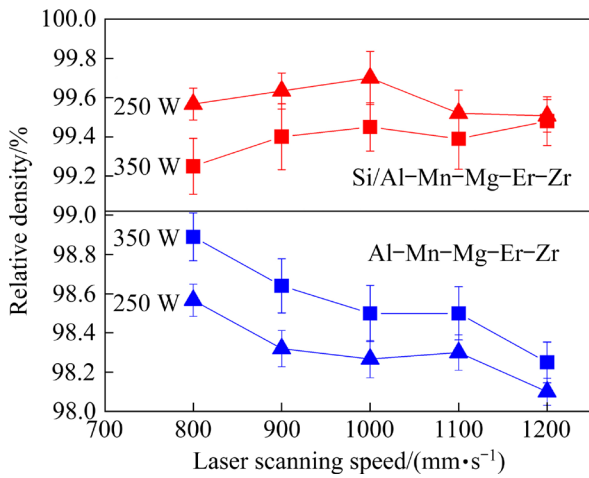

Fig. 5 Relative density of Al−Mn−Mg−Er−Zr and Si/Al−Mn−Mg−Er−Zr samples fabricated with different process parameters

Al−Mn−Mg−Er−Zr alloy (Fig. 7(a)). After the Si alloying, a new Mg$_2$Si phase was formed (Fig. 7(a)). The DTA cooling curves of the alloy are shown in Fig. 7(b). The solidification temperature decreased by 20 °C (from 642 °C for Al−Mn−Mg−Er−Zr alloy to 622 °C for Si/Al−Mn−Mg−Er−Zr alloy). A single eutectic point was observed at 612 °C for Al−Mn−Mg−Er−Zr alloy. For Si/Al−Mn−Mg−Er−Zr alloy, the first eutectic point shifted to a lower temperature, and a second separate eutectic peak appeared at a lower temperature (568 °C).

According to the XRD patterns (Fig. 7(a)) and previous reports [19,20], the second eutectic peak was determined to represent the solidification of eutectic Al−Mg$_2$Si.

Figure 8 shows the EBSD orientation maps, pole figure (PF), and grain size distribution of the SLM-fabricated Al−Mn−Mg−Er−Zr and Si/Al−Mn−Mg−Er−Zr alloys. The SLM-fabricated Si/Al−Mn−Mg−Er−Zr alloy presented finer and more equiaxed grains at the melt pool boundaries. The intensity of the ⟨100⟩ texture of α(Al) and both the length and width of the columnar grains were reduced after Si alloying (Figs. 8(a, b)). As a result, the SLM-fabricated Si/Al−Mn−Mg−Er−Zr alloy showed a smaller grain size (4.66 μm) than SLM-fabricated Al−Mn−Mg−Er−Zr alloy (~5.10 μm), as shown in Figs. 8(c, d).

3.4 Tensile properties

The engineering tensile stress−strain curves of the SLM-fabricated Si/Al−Mn−Mg−Er−Zr samples are shown in Fig. 9(a). The values of the YS, UTS, and elongation obtained from the stress−strain curves were (371±7) MPa, (518±6) MPa, and (5±0.3)%, respectively. Compared with the SLM-fabricated Al−Mn−Mg−Er−Zr alloy, the YS and UTS increased by 44 MPa and 16 MPa, respectively, but the elongation decreased significantly [16], as
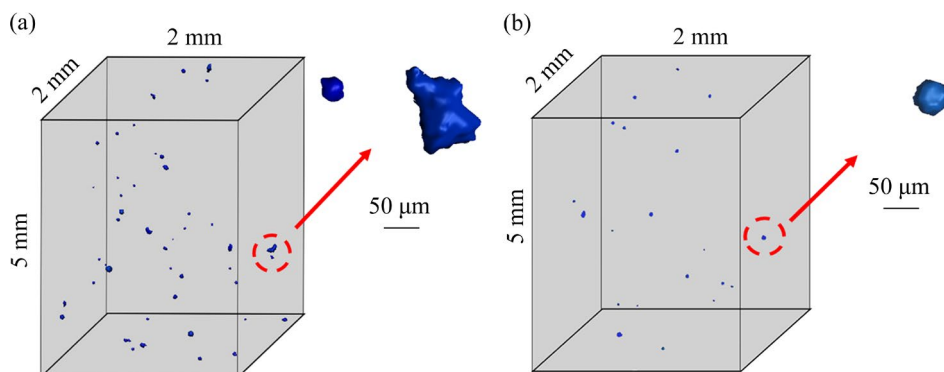
Fig. 6 Observation of internal pores by CT of SLM-fabricated Al−Mn−Mg−Er−Zr (a) and Si/Al−Mn−Mg−Er−Zr (b) samples
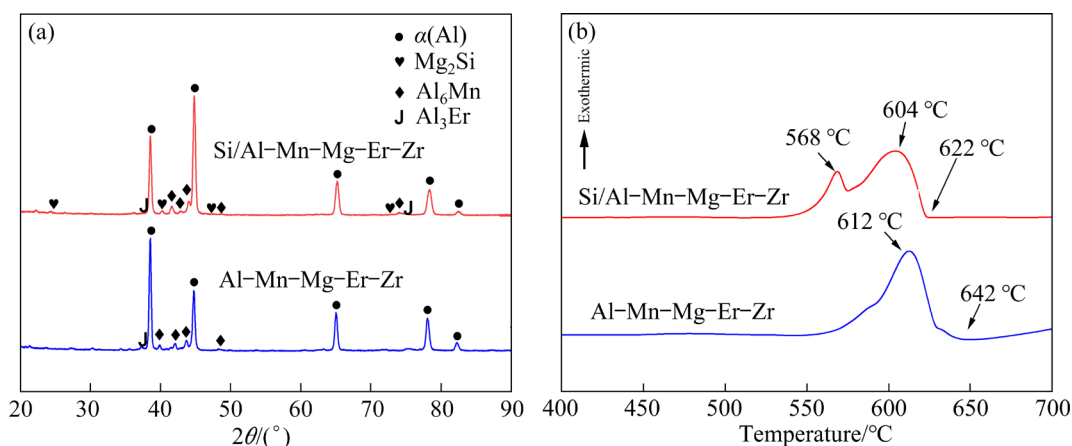

Fig. 7 XRD patterns (a) and DTA curves (b) of SLM-fabricated Al−Mn−Mg−Er−Zr and Si/Al−Mn−Mg−Er−Zr samples

shown in Fig. 9(b). The strength of the alloy was also higher than that of other SLM-fabricated Sc-free Al−Mg-based alloys [21,22].

4 Discussion

4.1 Effect of Si on balling and processability

Compared with the Al−Mn−Mg−Er−Zr alloy, surface balling did not exist in the Si/Al−Mn−Mg−Er−Zr alloy obtained from SLM. Laser spatter was the main reason for the spheroidization of the SLM-deposited alloy surface [23]. Laser spatter was created in the form of droplets expelled from the melt pool, which were oxidized in-flight before landing on the powder bed [24,25]. WANG et al [26] reported that the addition of Si to an Al−Cu−Mg alloy enhanced the laser absorptivity of aluminum alloy. GHASEMI et al [27] measured the laser absorptivity of pure Al, AlSi10Mg, and AlSi12 alloys. The result showed that the laser absorptivity of AlSi12 was 51% higher than that of pure Al. The

mixing of Si with an Al−Mn−Mg−Er−Zr alloy increased the laser absorptivity of the powder. A higher laser absorption resulted in a higher temperature within the melt pool with the same process parameters. This decreased the viscosity of the melt, enabling the liquid to spread and ultimately improving the bonding of alloy [28]. In addition, the formation of low-temperature Al−Mg$_2$Si eutectic and a decrease in the solidification temperature of the Si/Al−Mn−Mg−Er−Zr alloy further reduced the viscosity and surface tension of the melt. The metal droplets induced by laser spatter with a low melting point and high fluidity were easier to spread after falling back to the surface of the molten pool (Fig. 3), thus reducing the possibility of balling.

The high surface roughness of the SLM-fabricated Al−Mn−Mg−Er−Zr alloy was mostly due to balling induced by laser spatter [29]. First, if these balls landed in an area where a part was fabricated, they could have become trapped and
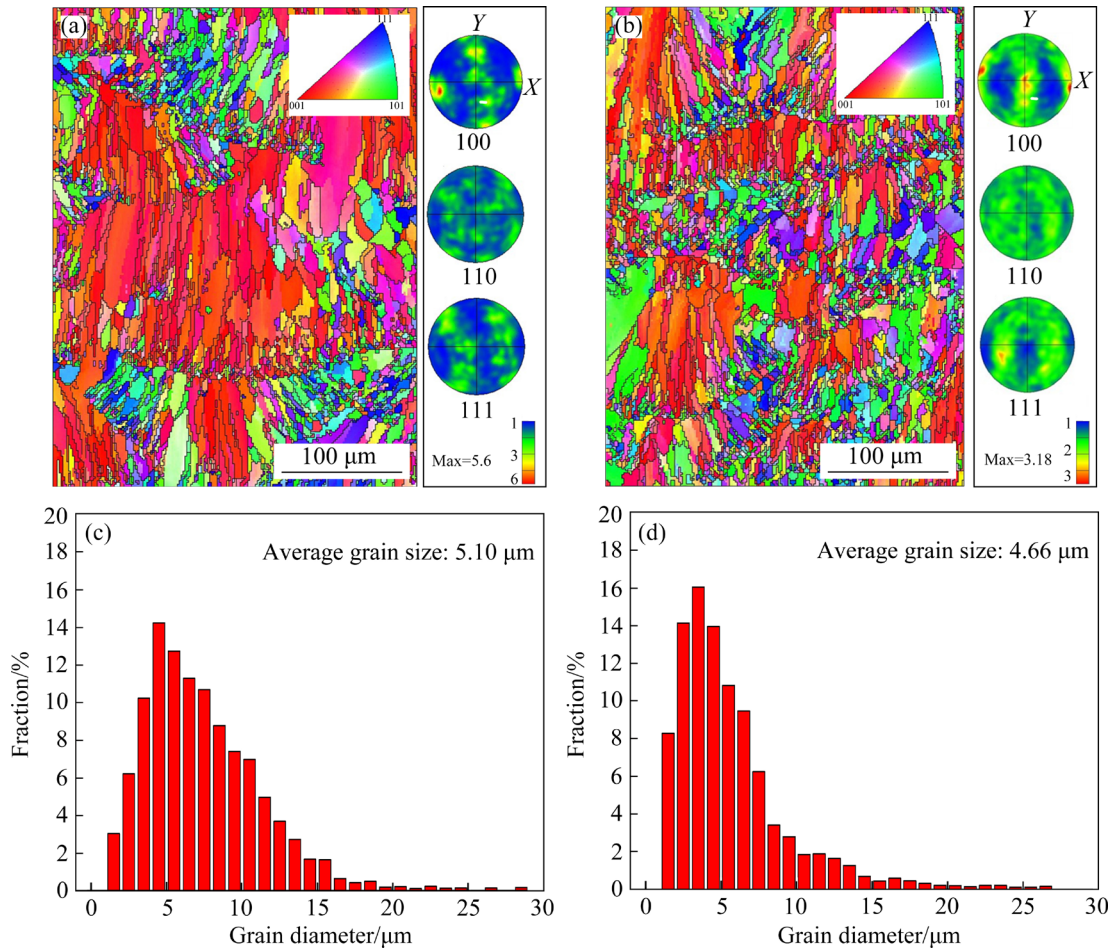
Fig. 8 EBSD orientation maps (a, b) and grain size distribution (c, d) of SLM-fabricated Al−Mn−Mg−Er−Zr (a, c) and Si/Al−Mn−Mg−Er−Zr (b, d) samples
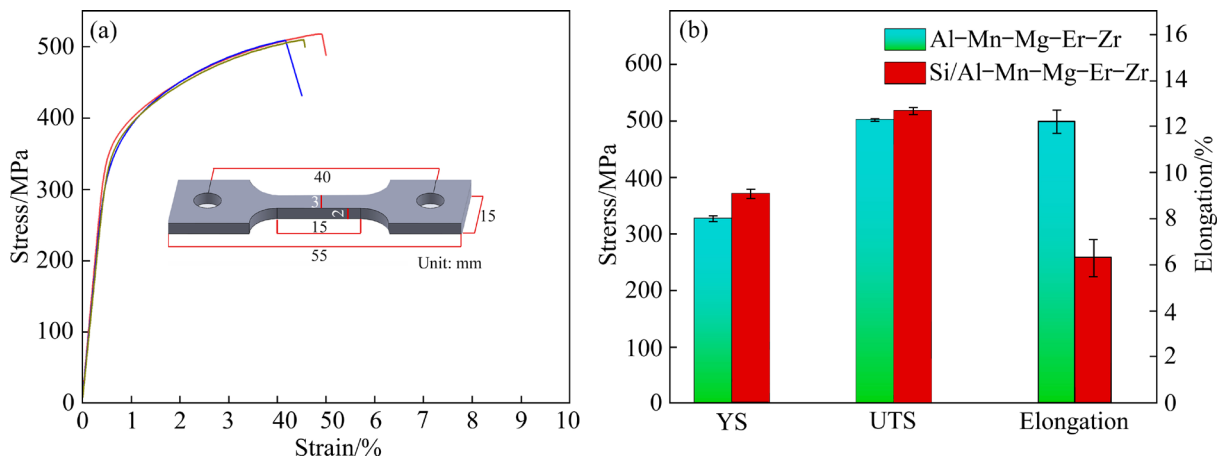

Fig. 9 Tensile stress−strain curves of Si/Al−Mn−Mg−Er−Zr alloy fabricated at 250 W and 1000 mm/s (a), and comparison of mechanical properties of SLM-fabricated Al−Mn−Mg−Er−Zr and Si/Al−Mn−Mg−Er−Zr samples (b)

acted as a contaminant that did not completely melt during re-melting while processing the following layers [23]. Second, excessive balling prevented the uniform deposition of powder layers. These phenomena caused the melt to incompletely fill the

gaps of the irregular surface [30]. As a result, keyholes were formed in the alloy (Figs. 4(a) and 6(a)), which decreased its processability and mechanical properties [31,32]. SLM parts often experience more thermally-induced residual stresses

due to the fast cooling rate of SLM [24]. Once a keyhole is formed, residual stresses easily concentrate in irregular regions and cracks are formed when the residual stress exceeds the yield strength of the material during solidification (Figs. 2(a) and 4(a)).

After Si alloying, the absence of balling on the alloy surface prevented the formation of keyholes and reduced the crack sensitivity and porosity of the alloy (Figs. 4(b) and 6(b)). The microstructure also greatly influenced the formation of cracks in the SLM-fabricated alloy. Many studies have indicated that grain refinement can prevent the generation of cracks and increase the processability of the alloys [33−35]. As potent nucleation sites, solutes contribute to grain refinement via the generation of a constitutional supercooling zone at the solid− liquid interface front, which restricts grain growth when heterogeneous nucleation occurs within the constitutional supercooling zone [36]. The nucleation efficiency of a solute can be evaluated by the growth restriction factor (Q), which is expressed as follows [37]:

$$Q=m(k-1)C_0 \tag{1}$$

where m, k, and C_0 represent the slope of the liquidus, partition coefficient, and solute concentration, respectively. Solutes with a large Q value rapidly generate constitutional supercooling at the solid−liquid interface front, leading to substantial grain refinement. The addition of Si to the Al−Mn−Mg−Er−Zr alloy increased the Q value [5] and decreased the grain size of SLM-fabricated Si/Al−Mn−Mg−Er−Zr alloy (Fig. 8(b)). The greater number of fine equiaxed grains and smaller grain size in the SLM-fabricated Si/Al−Mn−Mg−Er−Zr alloy increased the total grain boundary surface area within a given volume, which toughened the matrix and avoided inter-granular cracking [20]. Finally, Si reduced the solidification temperature and an Al−Mg₂Si eutectic was formed in the Si/Al−Mn−Mg−Er−Zr alloy. The lower solidification temperature and better fluidity of the melt may have backfilled cracks during the final stage of solidification, which also reduced the crack sensitivity of the alloy [17−19,26]. Overall, the absence of balling and keyholes, the refined grain size, the lower solidification temperature, and the improved fluidity of the melt all contributed to the good processability of the SLM-fabricated Si/Al−Mn−Mg−Er−Zr alloy.

4.2 Effect of Si on mechanical properties

It was shown that Si alloying remarkably increased the strength of the alloy. The YS increased from (327±5) MPa for the Al−Mn−Mg− Er−Zr alloy to (371±7) MPa for the Si/Al−Mn− Mg−Er−Zr alloy. Compared with the SLM-fabricated Al−Mn−Mg−Er−Zr alloy, the grain size of the SLM-fabricated Si/Al−Mn−Mg−Er−Zr alloy was finer (Fig. 8). It has long been established that the strength of polycrystalline metals can be greatly enhanced by tailoring grain structures down to the sub-micron or even nanometer scale following the classic Hall−Petch relationship [38]. The strengthening effect arises from substantially hindered dislocation motion by the introduction of a high density of grain boundaries [4]. The precipitation of the Mg₂Si phase also helped increase the strength of the alloy following Orowan dislocation looping in the SLM-fabricated Si/Al− Mn−Mg−Er−Zr alloy. However, the formation of an Al−Mg₂Si eutectic microstructure deteriorated the ductility of the alloy due to the brittle nature of the large Mg₂Si phase [5,39,40].

5 Conclusions

(1) Alloying with Si element eliminated balling and reduced the surface roughness of the alloy, thus avoiding the generation of keyholes in the SLM-fabricated Si/Al−Mn−Mg−Er−Zr alloy. The introduction of Si also refined the grain size, reduced the solidification temperature, and an Al−Mg₂Si eutectic structure with a low melting point was formed. These factors reduced the crack sensitivity and greatly increased the processability of the alloy.

(2) The relative density of all SLM-fabricated Si/Al−Mn−Mg−Er−Zr alloys exceeded 99.2%, which was much higher than that of the Si-free alloy (<99%). The sample fabricated at a laser power of 250 W and scanning speed of 1000 mm/s exhibited a maximum relative density of 99.6%, showing good processability.

(3) Compared with the SLM-fabricated Al−Mn−Mg−Er−Zr alloy, the SLM-fabricated Si/Al−Mn−Mg−Er−Zr alloy had a higher strength due to fine-grain strengthening and precipitation strengthening.

CRediT authorship contribution statement

Jiang YU: Writing – Review & editing, Methodology, Data curation; **Yao-xiang GENG:** Methodology, Validation, Formal analysis, Investigation, Data curation, Writing – Original draft, Writing – Review & editing; **Hong-bo JU:** Data curation; **Zhi-jie ZHANG:** Data curation; **Jun-hua XU:** Funding acquisition, Project administration.

Declaration of competing interest

The authors declare that they have no known competing financial interests or personal relationships that could have appeared to influence the work reported in this paper.

Acknowledgments

References

[1] GENG Yao-xiang, WANG Ying-min, XU Jun-hua, MI Shao-bo, FAN Shi-min, XIAO Ya-kai, WU Yi, LUAN Jun-hua. A high-strength AlSiMg1.4 alloy fabricated by selective laser melting [J]. Journal of Alloys and Compounds, 2021, 867: 159103.

[2] GENG Yao-xiang, WANG Qing, WANG Ying-min, ZANG Qian-hao, MI Shao-bo, XU Jun-hua, XIAO Ya-kai, WU Yi, LUAN Jun-hua. Microstructural evolution and strengthening mechanism of high-strength AlSi8.1Mg1.4 alloy produced by selective laser melting [J]. Materials & Design, 2022, 218: 110674.

[3] WANG Pei, ECKERT J, PRASHANTH K G, WU Ming-wei, KABAN I, XI Li-xia, SCUDINO S. A review of particulate-reinforced aluminum matrix composites fabricated by selective laser melting [J]. Transactions of Nonferrous Metals Society of China, 2020, 30(8): 2001−2034.

[4] JIA Qing-bo, ROMETSCH P, KÜRNSTEINER P, CHAO Qi, HUANG Ai-jun, WEYLAND M, BOURGEOIS L, WU Xin-hua. Selective laser melting of a high strength Al−Mn−Sc alloy: Alloy design and strengthening mechanisms [J]. Acta Materialia, 2019, 171: 108−118.

[5] LI Rui-di, WANG Min-bo, LI Zhi-ming, CAO Peng, YUAN Tie-chui, ZHOU Hong-bin. Developing a high-strength Al−Mg−Si−Sc−Zr alloy for selective laser melting: Crack-inhibiting and multiple strengthening mechanisms [J]. Acta Materialia, 2020, 193: 83−98.

[6] JIA Qing-bo, ZHANG Fan, ROMETSCH P, LI Jing-wei, MATA J, WEYLAND M, BOURGEOIS L, SUI Man-ling, WU Xin-hua. Precipitation kinetics, microstructure evolution and mechanical behavior of a developed Al−Mn−Sc alloy fabricated by selective laser melting [J]. Acta Materialia, 2020, 193: 239−251.

[7] SCHMIDTKE K, PALM F, HAWKINS A, EMMELMANN C. Process and mechanical properties: Applicability of a scandium modified Al-alloy for laser additive manufacturing [J]. Physics Procedia, 2011, 12: 369−374.

[8] SPIERINGS A B, DAWSON K, UGGOWITZER P J, WEGENER K. Influence of SLM scanspeed on microstructure, precipitation of Al_3Sc particles and mechanical properties in Sc- and Zr-modified Al−Mg alloys [J]. Materials & Design, 2018, 140: 134−143.

[9] KULITSKIY V, MALOPHEYEV S, KAIBYSHEV R. Effect of cold rolling on microstructure and mechanical properties of an Al−Mg−Sc−Zr alloy [J]. Advanced Materials Research, 2014, 922: 388−393.

[10] GENG Yao-xiang, TANG Hao, XU Jun-hua, ZHANG Zhi-jie, XIAO Ya-kai, WU Yi. Strengthening mechanisms of high-performance Al−Mn−Mg−Sc−Zr alloy fabricated by selective laser melting [J]. Science China Materials, 2021, 64(12): 3131−3137.

[11] TANG Hao, GENG Yao-xiang, BIAN Shu-nuo, XU Jun-hua, ZHANG Zhi-jie. An ultra-high strength over 700 MPa in Al−Mn−Mg−Sc−Zr alloy fabricated by selective laser melting [J]. Acta Metallurgica Sinica (English Letters), 2022, 35: 466−474.

[12] GENG Yao-xiang, TANG Hao, XU Jun-hua, ZHANG Zhi-jie, YU Li-huan, JU Hong-bo, JIANG Le, JIAN Jiang-lin. Formability and mechanical properties of high strength Al-(Mn,Mg)-(Sc,Zr) alloy produced by selective laser melting [J]. Acta Metallurgica Sinica, 2022, 58(8): 1044−1054.

[13] JIA Qing-bo, ROMETSCH Paul, CAO Sheng, ZHANG Kai, HUANG Ai-jun, WU Xin-hua. Characterisation of AlScZr and AlErZr alloys processed by rapid laser melting [J]. Scripta Materialia, 2018, 151, 42−46.

[14] WU Hao, WEN Sheng-ping, LU Jun-tai, MI Zhen-peng, ZENG Xian-long, HUANG Hui, NIE Zuo-ren. Micro-structural evolution of new type Al−Zn−Mg−Cu alloy with Er and Zr additions during homogenization [J]. Transactions of Nonferrous Metals Society of China, 2017, 27(7): 1476−1482.

[15] WANG Shao-hua, MENG Ling-gang, YANG Shou-jie, FANG Can-feng, HAO Hai, DAI Sheng-long, ZHANG Xing-guo. Microstructure of Al−Zn−Mg−Cu−Zr−0.5Er alloy under as-cast and homogenization conditions [J]. Transactions of Nonferrous Metals Society of China, 2011, 21(7): 1449−1454.

[16] GENG Yao-xiang, JIA Chao-gang, XU Jun-hua, ZHANG Zhi-jie, JU Hong-bo, WANG Dong-peng, YU Li-huan. Selective laser melting of a novel high-strength Er- and Zr-modified Al−Mn−Mg alloy [J]. Materials Letters, 2022, 313: 131762.

[17] WANG Pei, GAMMER C, BRENNE F, PRASHANTH K G, MENDES R G, RÜMMELI M H, GEMMING T, ECKERT J, SCUDINO S. Microstructure and mechanical properties of a heat-treatable Al−3.5Cu1.5Mg−1Si alloy produced by selective laser melting [J]. Materials Science and Engineering A, 2018, 711: 562−570.

[18] OTANI Y, SASAKI S. Effects of the addition of silicon to 7075 aluminum alloy on microstructure, mechanical

properties, and selective laser melting processability [J]. Materials Science and Engineering A, 2020, 777: 139079.

[19] LI Lan-bo, LI Rui-di, YUAN Tie-chui, CHEN Chao, ZHANG Zhi-jian, LI Xiao-feng. Microstructures and tensile properties of a selective laser melted Al−Zn−Mg−Cu (Al7075) alloy by Si and Zr microalloying [J]. Materials Science and Engineering A, 2020, 787: 139492.

[20] MONTERO-SISTIAGA M L, MERTENS R, VRANCKEN B, WANG Xie-bin, HOOREWEDER V B, KRUTH J P, HUMBEECK V J. Changing the alloy composition of Al7075 for better processability by selective laser melting [J]. Journal of Materials Processing Technology, 2016, 238: 437−445.

[21] CROTEAU J R, GRIFFITHS S, ROSSELL M D, LEINENBACH C, KENEL C, JANSEN V, SEIDMAN D N, DUNAND D C, VO N Q. Microstructure and mechanical properties of Al−Mg−Zr alloys processed by selective laser melting [J]. Acta Materialia, 2018, 153: 35−44.

[22] ZHOU Le, HYER H, PARK S, PAN Hao, BAI Yuan-li, RICE K P, SOHN Y. Microstructure and mechanical properties of Zr-modified aluminum alloy 5083 manufactured by laser powder bed fusion [J]. Additive Manufacturing, 2019, 28: 485−496.

[23] LY S, RUBENCHIK A M, KHAIRALLAH S A, GUSS G, MATTHEWS M J. Metal vapor micro-jet controls material redistribution in laser powder bed fusion additive manufacturing [J]. Scientific Reports, 2017, 7: 4085.

[24] ABOULKHAIR N T, SIMONELLI M, PARRY L, ASHCROFT I, TUCK C, HAGUE R. 3D printing of aluminium alloys: Additive manufacturing of aluminium alloys using selective laser melting [J]. Progress in Materials Science, 2019, 106: 100578.

[25] SIMONELLI M, TUCK C, ABOULKHAIR N T, MASKERY I, ASHCROFT I, WILDMAN R D, HAGUE R. A Study on the laser spatter and the oxidation reactions during selective laser melting of 316L stainless steel, Al−Si10−Mg, and Ti−6Al−4V [J]. Metallurgical Materials Transactions A, 2015, 46: 3842−3851.

[26] WANG Q Z, KANG N, LIN X, MANSORI M E L, LIU Y, LU J L, WANG Y F, CHAI H Z, HUANG W D. On the Si-induced microstructure evolution, solidification cracking healing and strengthening behavior of laser powder bed fusion additive manufactured Al−Cu−Mg/Si alloys [J]. Journal of Materials Processing Technology, 2023, 313: 117860.

[27] GHASEMI A, FEREIDUNI E, BALBAA M, JADHAV S D, ELBESTAWI M, HABIBI S. Influence of alloying elements on laser powder bed fusion processability of aluminum: A new insight into the oxidation tendency [J]. Additive Manufacturing, 2021, 46: 102145.

[28] LI Ya-li, GU Dong-dong. Parametric analysis of thermal behavior during selective laser melting additive manufacturing of aluminum alloy powder [J]. Materials & Design, 2014, 63: 856−867.

[29] MOWER T M, LONG M J. Mechanical behavior of additive

manufactured, powder-bed laser-fused materials [J]. Materials Science and Engineering A, 2016, 651: 198−213.

[30] MASKERY I, ABOULKHAIR N T, CORFIELD M R, TUCK C, CLARE A T, LEACH R K, WILDMAN R D, ASHCROFT I A, HAGUE R J M. Quantification and characterisation of porosity in selectively laser melted Al−Si10−Mg using X-ray computed tomography [J]. Materials Characterization, 2016, 111: 193−204.

[31] WANG Lin-zhi, WANG Sen, WU Jiao-jiao. Experimental investigation on densification behavior and surface roughness of AlSi10Mg powders produced by selective laser melting [J]. Optics & Laser Technology, 2017, 96: 88−96.

[32] BIDARE P, BITHARAS I, WARD R M, ATTALLAH M M, MOORE A J. Fluid and particle dynamics in laser powder bed fusion [J]. Acta Materialia, 2018, 142: 107−120.

[33] CHENG Wei, LIU Yun-zhong, XIAO Xiao-jun, HUANG Bin, ZHOU Zhi-guang, LIU Xiao-hui. Microstructure and mechanical properties of a novel (TiB$_2$+TiC)/AlSi10Mg composite prepared by selective laser melting [J]. Materials Science and Engineering A, 2022, 834: 142435.

[34] WANG Yan-fang, LIN Xin, KANG Nan, WANG Zi-hong, WANG Qing-zheng, LIU Yu-xin, HUANG Wei-dong. Laser powder bed fusion of Zr-modified Al−Cu−Mg alloy: Crack-inhibiting, grain refinement, and mechanical properties [J]. Materials Science and Engineering A, 2022, 838: 142618.

[35] SUN Teng-teng, WANG Hong-ze, GAO Zhen-yang, WU Yi, WANG Ming-liang, JIN Xin-yuan, LEUNG C L A, LEE P D, FU Ya-nan, WANG Hao-wei. The role of in-situ nano-TiB$_2$ particles in improving the printability of noncastable 2024Al alloy [J]. Materials Research Letters, 2022, 10(10): 656−665.

[36] TAN Qi-yang, ZHANG Jing-qi, SUN Qiang, FAN Zhi-qi, LI Gan, YIN Yu, LIU Yin-gang, ZHANG Ming-xing. Inoculation treatment of an additively manufactured 2024 aluminium alloy with titanium nanoparticles [J]. Acta Materialia, 2020, 196: 1−16.

[37] STJOHN D H, QIAN M, EASTON M A, CAO P. The interdependence theory: The relationship between grain formation and nucleant selection [J]. Acta Materialia, 2011, 59(12): 4907−4921.

[38] HU J, SHI Y N, SAUVAGE X, SHA G, LU K. Grain boundary stability governs hardening and softening in extremely fine nanograined metals [J]. Science, 2017, 355(6331): 1292−1296.

[39] BHANDARI R, BISWAS P, MALLIK M, MONDAL M K. Microstructure based numerical simulation of the micromechanics and fracture in hypereutectic Al−Mg$_2$Si composites [J]. Materials Chemistry and Physics, 2023, 297: 127427.

[40] LI Bo, WANG Kai, LIU Ming-xiang, XUE Han-song, ZHU Zi-zong, LIU Chang-ming. Effects of temperature on fracture behavior of Al-based in-situ composites reinforced with Mg$_2$Si and Si particles fabricated by centrifugal casting [J]. Transactions of Nonferrous Metals Society of China, 2013, 23(4): 923−930.

激光选区熔化 Si 改性 Al–Mn–Mg–Er–Zr 合金
裂纹消除及强化机理

于 江 [1]，耿遥祥 [1]，鞠洪博 [1,2]，张志杰 [1]，许俊华 [1]

1. 江苏科技大学 材料科学与工程学院，镇江 212100；

2. Department of Mechanical Engineering, CEMMPRE-Centre for Mechanical Engineering Materials and Processes, University of Coimbra, Coimbra, Portugal

摘 要：为了提升激光选区熔化(SLM)成形 Al–Mn–Mg–Er–Zr 合金的成形性和工艺窗口，应用 SLM 技术制备 Si 改性的 Al–Mn–Mg–Er–Zr 合金，系统研究 Si 合金化对合金表面质量、成形性、显微组织和力学性能的影响。结果表明，Si 的合金化能有效抑制合金的表面球化现象及未熔合孔的产生，细化合金的晶粒尺寸，降低合金的凝固温度，并形成 Al–Mg$_2$Si 低熔点共晶组织，从而有效抑制合金成形过程中热裂纹的产生，提升合金的成形性和工艺窗口。SLM 成形 Si/Al–Mg–Mn–Er–Zr 合金的最大相对密度为 99.6%。该 SLM 成形合金的屈服和抗拉强度分别为(371±7) MPa 和(518±6) MPa，高于目前报道的 SLM 成形 Al–Mg–Mn–Er–Zr 及其他 SLM 成形非 Sc 改性 Al–Mg 基合金。

关键词：激光选区熔化；Al–Mn–Mg–Er–Zr–Si 合金；表面粗糙度；成形性；力学性能

(Edited by Bing YANG)